

Can a non-ideal metal ferromagnet inject spin into a semiconductor with 100% efficiency without a tunnel barrier?

J. Wan, M. Cahay

Department of Electrical and Computer Engineering and Computer Science
University of Cincinnati, Cincinnati, Ohio 45221

S. Bandyopadhyay

Department of Electrical and Computer Engineering
Virginia Commonwealth University, Richmond, Virginia 23284

ABSTRACT

Current understanding of spin injection tells us that a metal ferromagnet can inject spin into a semiconductor with 100% efficiency if either the ferromagnet is an ideal half metal with 100% spin polarization, or there exists a suitable tunnel barrier at the interface. In this paper, we show that, at absolute zero temperature, 100% spin injection efficiency from a *non-ideal* metal ferromagnet into a semiconductor quantum wire can be reached at certain injection energies, *without* a tunnel barrier, provided there is an axial magnetic field along the direction of current flow as well as a spin orbit interaction in the semiconductor. At these injection energies, spin is injected *only* from the majority spin band of the ferromagnetic contact, resulting in 100% spin injection efficiency. This happens because of the presence of antiresonances in the transmission coefficient of the minority spins when their incident energies coincide with Zeeman energy states in the quantum wire. At absolute zero and below a critical value of the axial magnetic field, there are two distinct Zeeman energy states and therefore two injection energies at which ideal spin filtering is possible; above the

critical magnetic field there is only one such injection energy. The spin injection efficiency rapidly decreases as the temperature increases. The rate of decrease is slower when the magnetic field is above the critical value. The appropriate choice of semiconductor materials and structures necessary to maintain a large spin injection efficiency at elevated temperatures is discussed.

I. INTRODUCTION

The problem of spin injection across a ferromagnetic/semiconductor (Fe/Sm) interface has received increasing attention over the last ten years with the advent of spintronics. Several recent experimental investigations have shown successful spin injection into semiconductor heterostructures from ferromagnetic metals using tunnel barriers in the form of Schottky contacts [1, 2, 3], thin metal oxides [4, 5, 6], or AlAs barriers [7]. A spin injection efficiency of about 70 % has been recently demonstrated using a CoFe/MgO tunnel contact to a GaAs layer [6]. Simultaneously, several theoretical models have been developed to understand the mechanisms controlling spin injection across specular and disordered Fe/Sm interfaces, some of which have been based on a simple Stoner model of the ferromagnetic contact [8, 9, 10] while others have included the full electronic band structure of the contact [11, 12].

It is currently believed that if the ferromagnet is metallic and there is no tunnel barrier between the ferromagnet and the semiconductor, then the infamous “resistance mismatch” problem will preclude a high spin injection efficiency unless the ferromagnet is an ideal half metal with 100 % spin polarization [9, 13]. Here we show that 100 % spin injection efficiency is possible at absolute zero temperature from a metallic ferromagnet with less than 100 % spin polarization into a semiconductor quantum wire, in spite of a resistance mismatch and in spite of the absence of any tunnel barrier, as long as there is an axial magnetic field along the wire and a Rashba spin orbit interaction [14] in the semiconductor. The 100% efficiency is obtained only for certain injection energies. At temperatures $T > 0$ K, thermal smearing will cause the energy-averaged spin injection efficiency to be much less than 100%. This problem can be mitigated by injecting through a double barrier resonant tunneling diode whose transmission peak is narrow and matched to the required injection energy. This approach results in a nearly monochromatic injection even at elevated temperatures. Accordingly, a high injection efficiency can be maintained even for $T > 0$ K.

This paper is organized as follows. In Section 2, we calculate the spin-dependent contact conductance between a non-ideal metallic ferromagnetic contact and a quasi one-dimensional semiconducting wire formed using a combination of mesa etching and electrostatic confinement as shown in Fig. 1. This problem is of relevance considering the many experimental efforts to realize Spin Field Effect Transistors [15].

1 Spin dependent interface conductance

The structure that we consider is shown in Fig. 1. The ferromagnetic contact that injects electrons into the quantum wire (which we call the source contact) is quasi one-dimensional, but the extracting contact (which we call the drain contact) is a two-dimensional electron gas to which the quantum wire opens up on the right. The questions we address are: in the linear mode of operation (i.e., for a small bias between the source and drain contact) how is the contact resistance of the Fe/Sm interface affected by the presence of the Rashba interaction due to the heterostructure interface formed between materials I (narrow bandgap) and II (wide bandgap) in the semiconducting channel? How is that conductance affected by the presence of a magnetic field applied in the direction of current flow? The magnetic field can be either an external magnetic field or the stray magnetic field that exists in the vicinity of the Fe/Sm interface because of the magnetized source contact. In this paper, we consider an external magnetic field which has uniform strength along the length of the wire.

In ref. [16], we found that the energy dispersion relationships ($E-k_x$) for the lowest energy bands in the semiconducting channel have the general shape shown in Figure 2(a). As was shown in [16], close to the bottom of the lowest subband, the $E-k_x$ relationship has a camel-back shape. Here we will show that this is strictly valid for a magnetic field below some critical value B_c . Above that threshold, the $E-k_x$ relationships are as shown in Fig. 2(b) where the camel-back feature of the bottom

subband disappears.

If the potential applied to the gate in Fig. 1 is changed, the potential step between the bottom of the conduction band in the ferromagnetic layer and the bottom of the conduction band in the semiconductor quantum wire far from the interface (ΔE_c) will change. As a result, the Fermi level can be swept from below the energy level E_1 (bottom of the lower subband) to above E_3 (bottom of the upper subband).

Depending on whether the magnetic field is below or above the threshold value B_c , the following two possibilities will occur. Referring to Fig. 2(a) ($B < B_c$), if we start with a value of ΔE_c such that E_F is above E_3 , there will be initially two propagating modes in the semiconductor channel. When E_F is in the range $[E_2, E_3]$, the upper band will become an evanescent channel with a wavenumber which is equal to zero when E_F is exactly equal to E_3 or E_2 , whereas the lower subband is still conducting. In the energy range $[E_1, E_2]$, the two channels are conducting again and there should be a rise in conductance until E_F reaches E_1 . At that point, wavevectors corresponding to the Fermi energy in both subbands will be real, equal and *finite*. With a slight increase in ΔE_c , the Fermi level will fall below E_1 and both subbands will be evanescent. We therefore expect a sharp drop in the conductance as the Fermi level falls below E_1 and the semiconducting channel is completely pinched-off.

For the case where the magnetic field is above the critical value B_c , the interface conductance should show a kink as the Fermi level is swept from above to below the threshold energy E_3 . Since the upper mode stays evanescent after E_F drops from E_3 to E_1 and the lower mode has a propagating wavevector which gradually shrinks to zero as E_F approaches E_1 , the conductance of the interface should smoothly approach zero as the channel is being pinched-off, contrary to the previous case.

The above discussion pertains to temperature $T = 0$ K. At elevated temperatures, the effect of thermal averaging will smooth out any of the abrupt features in the conductance versus gate voltage characteristics discussed above. At finite temperature

and for low value of the bias across the interface (linear mode of operation), the conductance of the interface due to the majority spin is given by

$$G_{\uparrow} = \frac{e^2}{4h k_B T} \int_0^{\infty} T_{\uparrow} \operatorname{sech}^2\left(\frac{E - E_F}{2k_B T}\right) dE, \quad (1)$$

where T_{\uparrow} is the total transmission coefficient of the majority spin incident from the contact and E is the energy of the electron incident from the ferromagnetic contact. A similar expression is used to calculate the conductance of the minority spin band by replacing T_{\uparrow} by T_{\downarrow} . The total conductance of the interface G_{tot} is then equal to $G_{\uparrow} + G_{\downarrow}$ since the two spin states are orthogonal in the contacts.

In this paper, we investigate the influence of an axial magnetic field and finite temperature on the spin injection efficiency (η) of the Fe/Sm quantum wire interface which is defined as follows

$$\eta = \frac{I_{\uparrow} - I_{\downarrow}}{I_{\uparrow} + I_{\downarrow}} = \frac{G_{\uparrow} - G_{\downarrow}}{G_{\uparrow} + G_{\downarrow}}. \quad (2)$$

where I_{\uparrow} and I_{\downarrow} are the spin polarized currents.

1.1 Dispersion relations

The single particle effective-mass Hamiltonian describing the quantum wire subjected to an axial magnetic field and Rashba spin orbit interaction is [17]

$$H = \frac{1}{2m^*} \left(\vec{p} + e\vec{A} \right)^2 + V_1(y) + V_2(z) + (g^*/2)\mu_B \vec{B} \cdot \vec{\sigma} + \frac{\alpha_R}{\hbar} \hat{y} \cdot \left[\vec{\sigma} \times (\vec{p} + e\vec{A}) \right] \quad (3)$$

where \hat{y} is the unit vector normal to the heterostructure interface in Fig. 1, \vec{A} is the vector potential due to the axial magnetic field \vec{B} along the channel, and g^* the Landé factor in the channel [18]. The quantity α_R is the Rashba spin-orbit coupling constant which varies with the applied potential on the gate [19]. We will assume that the confining potentials along the y- and z-directions are $V_1(y)$ and $V_2(z)$ with the latter being parabolic.

The choice of the Landau gauge $\vec{A} = (0, -Bz, 0)$ allows us to decouple the y-component of the Hamiltonian in (3) from the x-z component. Accordingly, the two-dimensional Hamiltonian in the plane of the channel (x-z plane) is

$$H_{xz} = \frac{p_z^2}{2m^*} + \Delta E_c + \frac{1}{2}m^* (\omega_0^2 + \omega_c^2) z^2 + \frac{\hbar^2 k_x^2}{2m^*} + \frac{\hbar^2 k_R k_x}{m^*} \sigma_z + (g^*/2)\mu_B B \sigma_x - \frac{\hbar k_R p_z}{m^*} \sigma_x \quad (4)$$

where ω_0 is the curvature of the confining potential in the z-direction, $\omega_c = eB/m^*$, μ_B is the Bohr magneton, $k_R = m^* \alpha_R / \hbar^2$ is the Rashba wavevector, and ΔE_c is the potential barrier between the ferromagnet and semiconductor. We assume that ΔE_c includes the effects of the quantum confinement in the y-direction.

For a single moded structure, the energy dispersion relations in the channel can be derived from Equation (4). The first five terms of the Hamiltonian in Eq.(4) yield shifted parabolic subbands with dispersion relations:

$$E_{n,\uparrow} = (n+1/2)\hbar\omega + \Delta E_c + \frac{\hbar^2 k_x^2}{2m^*} + \frac{\hbar^2 k_R k_x}{m^*}, \quad E_{n,\downarrow} = (n+1/2)\hbar\omega + \Delta E_c + \frac{\hbar^2 k_x^2}{2m^*} - \frac{\hbar^2 k_R k_x}{m^*}, \quad (5)$$

where $\omega = \sqrt{\omega_0^2 + \omega_c^2}$. In Eq.(5), the \uparrow and \downarrow arrows indicate $+z$ and $-z$ polarized spins (eigenstates of the σ_z operator) which are split by the Rashba effect (fifth term in Equation (4)). These subbands have definite spin quantizations axes along $+z$ and $-z$ directions.

The sixth and seventh terms in Eq.(4) induce a mixing between the $+z$ - and $-z$ -polarized spins. The sixth term originates from the magnetic field due to the ferromagnetic contacts and the seventh originates from the Rashba effect itself. The ratio of the sixth and seventh term can be shown to be of the order of $10^4 - 10^6$ for typical values of the relevant parameters. Therefore, we can neglect the seventh term in comparison with the sixth term.

To obtain an analytical expression for the dispersion relation corresponding to the first six terms in the Hamiltonian in Eq.(4), we derive a two-band dispersion relation in a truncated Hilbert space considering mixing between the two lowest unperturbed

subband states (namely the +z and -z spin states). Straightforward diagonalization of the Hamiltonian in Eq.(4) (minus the seventh term) in the basis of these two unperturbed states gives the following dispersion relations for the two subbands:

$$E_1(k_x) = \frac{1}{2}\hbar\omega + \Delta E_c + \frac{\hbar^2 k_x^2}{2m^*} - \sqrt{\left(\frac{\hbar^2 k_R k_x}{m^*}\right)^2 + \left(\frac{g^* \mu_B B}{2}\right)^2}, \quad (6)$$

$$E_2(k_x) = \frac{1}{2}\hbar\omega + \Delta E_c + \frac{\hbar^2 k_x^2}{2m^*} + \sqrt{\left(\frac{\hbar^2 k_R k_x}{m^*}\right)^2 + \left(\frac{g^* \mu_B B}{2}\right)^2}. \quad (7)$$

These dispersion relations are plotted schematically as solid lines in Fig. 2. $E_1(k_x)$ refers to the lower subband whereas $E_2(k_x)$ refers to the upper subband.

The upper subband $E_2(k_x)$ has a global minimum at $k_x = 0$ for all values of B-field and k_R . The location of the minimum is at an energy

$$E_3 = \frac{\hbar\omega}{2} + \Delta E_c + \frac{|g^*| \mu_B B}{2} \quad (8)$$

indicated on Fig.2. This energy corresponds to the upper Zeeman energy level in the semiconductor channel.

The lower subband $E_1(k_x)$ has a camel-back shape as long as the external magnetic field B is less than some critical value B_c . The latter can be obtained by setting the derivative of the $E - k_x$ relationship equal to zero. The local maximum is located at $k_x = 0$ whereas two local minima are located at

$$k_{min} = \pm k_R \sqrt{1 - \frac{1}{16} \left(\frac{g^* \mu_B B}{\delta_R}\right)^2}. \quad (9)$$

The quantity k_{min} is real only if the external magnetic field B is less than the critical value B_c given by

$$|g^*| \mu_B B_c = 4\delta_R, \quad (10)$$

i.e., when the Zeeman splitting is four times the Rashba spin splitting energy δ_R :

$$\delta_R = \frac{\hbar^2 k_R^2}{2m^*}. \quad (11)$$

The value of $E_1(k_x)$ at $k_x = 0$ corresponds to the lower Zeeman energy level in the semiconductor channel and is given by

$$E_2 = \frac{\hbar\omega}{2} + \Delta E_c - \frac{|g^*|\mu_B B}{2}, \quad (12)$$

whereas the value of the energy at the minima k_{min} is given by

$$E_1 = \frac{\hbar\omega}{2} + \Delta E_c - [\delta_R + \frac{(g^* \mu_B B)^2}{16\delta_R}]. \quad (13)$$

From Equations (6 - 7), we find that an electron with energy E has wavevectors in the two bands given by

$$k_{x,1} = \frac{1}{\hbar} \sqrt{2m^* \left(\frac{A + \sqrt{A^2 - 4C}}{2} \right)}, \quad k_{x,2} = \frac{1}{\hbar} \sqrt{2m^* \left(\frac{A - \sqrt{A^2 - 4C}}{2} \right)} \quad (14)$$

where

$$A = 2(E - \frac{\hbar\omega}{2} - \Delta E_c) + 4\delta_R, \quad C = (E - \frac{\hbar\omega}{2} - \Delta E_c)^2 - \beta^2, \quad \beta = |g^*|\mu_B B/2. \quad (15)$$

It is obvious that when the external magnetic field $B < B_c$, in the energy range between E_2 and E_3 , C is negative and $k_{x,1}$ is real while $k_{x,2}$ is purely imaginary. This means that there is only one propagating channel in this energy range (the other channel is evanescent). On the other hand, if E is between E_1 and E_2 , or if E is larger than E_3 , then both $k_{x,1}$ and $k_{x,2}$ are real, so that there are two propagating channels.

If $B > B_c$, E_1 is equal to E_2 since the bottom subband loses its camel-back shape and has only a minimum at $k_x = 0$. In that case, if E is between E_1 and E_3 , then A is negative and $k_{x,2}$ is purely imaginary while $k_{x,1}$ is real. Thus, there is only one propagating channel. If $E > E_3$, then both A and C are positive and $k_{x,2}$, $k_{x,1}$ are both real, so that there are two propagating channels.

If $E < E_1$, then there is no propagating channel and the conductance drops sharply towards zero.

The eigenspinors corresponding to the eigenvalues given in Eqns.(6-7) have the explicit forms [17]

$$\begin{bmatrix} C_1(k_{x,1}) \\ C'_1(k_{x,1}) \end{bmatrix} = \begin{bmatrix} \alpha(k_{x,1})/\gamma(k_{x,1}) \\ \beta/\gamma(k_{x,1}) \end{bmatrix}$$

$$\begin{bmatrix} C_2(k_{x,2}) \\ C'_2(k_{x,2}) \end{bmatrix} = \begin{bmatrix} -\beta/\gamma(k_{x,2}) \\ \alpha(k_{x,2})/\gamma(k_{x,2}) \end{bmatrix} \quad (16)$$

where the quantities α and γ are given by

$$\alpha(k_x) = \frac{\hbar^2 k_R k_x}{m^*} + \sqrt{\left(\frac{\hbar^2 k_R k_x}{m^*}\right)^2 + \beta^2}, \quad \gamma(k_x) = \sqrt{\alpha^2 + \beta^2}. \quad (17)$$

As pointed out in ref. [16], these eigenspinors are not +z-polarized state $\begin{bmatrix} 1 & 0 \end{bmatrix}^\dagger$, or -z-polarized state $\begin{bmatrix} 0 & 1 \end{bmatrix}^\dagger$ if the magnetic field $B \neq 0$. Thus, the magnetic field mixes spins and the +z or -z polarized states are no longer eigenstates in the semiconducting channel. Equations (16) also show that the spin quantization axis (eigenspinor) in any subband is not fixed and strongly depends on the wavevector k_x . Thus, an electron entering the semiconductor channel from the left ferromagnetic contact with +x-polarized spin, will not couple *equally* to +z and -z states. The relative coupling will depend on the electron's energy.

1.2 The transport problem across the interface:

We model the ferromagnetic contact by the Stoner-Wohlfarth model. The magnetization of the contact is assumed to be along the x-direction so that the majority carriers are +x-polarized electrons (as in ref. [15]) and minority carriers are -x-polarized. Their bands are offset by an exchange splitting energy Δ (Fig. 2). In the expression of the Hamiltonian in Eq.(4) we add an extra potential energy term $V_I(x)$ to represent an interfacial potential barrier between the metallic ferromagnetic contact and the semiconducting channel. Following Schäpers et. al. [20], we model the interface barrier as a delta-scatterer:

$$V_I(x) = V_0 \delta(x), \quad (18)$$

where V_0 is the strength of the scattering potential.

In the semiconducting quasi one-dimensional channel ($x > 0$), the x-component of the wavefunction at a position x along the channel is given by

$$\psi_{II}(x) = T_1 \begin{bmatrix} C_1(k_{x,1}) \\ C'_1(k_{x,1}) \end{bmatrix} e^{ik_{x,1}x} + T_2 \begin{bmatrix} C_2(k_{x,2}) \\ C'_2(k_{x,2}) \end{bmatrix} e^{ik_{x,2}x}, \quad (19)$$

where T_1 and T_2 are the transmission amplitudes into the two subbands given by Equations (6) and (7).

For an electron in the *majority spin band* in the left ferromagnetic contact (region I; $x < 0$), the electron is spin polarized in the $[1, 1]^\dagger$ subband and the x-component of the wavefunction is given by

$$\psi_I^{majority}(x) = \frac{1}{\sqrt{2}} \begin{bmatrix} 1 \\ 1 \end{bmatrix} e^{ik_x^u x} + \frac{R_1}{\sqrt{2}} \begin{bmatrix} 1 \\ 1 \end{bmatrix} e^{-ik_x^u x} + \frac{R_2}{\sqrt{2}} \begin{bmatrix} 1 \\ -1 \end{bmatrix} e^{-ik_x^d x}, \quad (20)$$

where R_1 is the reflection amplitude into the +x-polarized band and R_2 is the reflection amplitude in the -x-polarized band.

The wavevectors

$$k_x^u = \frac{1}{\hbar} \sqrt{2m_0 E_F}, \quad k_x^d = \frac{1}{\hbar} \sqrt{2m_0 (E_F - \Delta)}, \quad (21)$$

are the x components of the wavevectors in the +x (majority spin) and -x-polarized (minority spin) energy bands in the ferromagnet, respectively.

For an electron in the *minority spin band* in the left ferromagnetic contact (region I; $x < 0$), the electron is spin polarized in the $[1, -1]^\dagger$ subband and the x-component of the wavefunction is given by

$$\psi_I^{minority}(x) = \frac{1}{\sqrt{2}} \begin{bmatrix} 1 \\ -1 \end{bmatrix} e^{ik_x^u x} + \frac{R'_1}{\sqrt{2}} \begin{bmatrix} 1 \\ -1 \end{bmatrix} e^{-ik_x^u x} + \frac{R'_2}{\sqrt{2}} \begin{bmatrix} 1 \\ 1 \end{bmatrix} e^{-ik_x^d x}, \quad (22)$$

where R'_1 is the reflection amplitude into the -x-polarized band and R'_2 is the reflection amplitude in the +x-polarized band.

The four unknowns (R_1, R_2, T_1, T_2) or (R'_1, R'_2, T_1, T_2) are solutions of a 4x4 system of equations obtained by enforcing continuity of the wavefunction and the quantity

$$\mu \frac{d\psi}{dx}(-\epsilon) + \frac{2m_s^* V_0}{\hbar^2} \psi(0) = \frac{d\psi}{dx}(+\epsilon) + ik_R(+\epsilon) \sigma_z \psi(+\epsilon), \quad (23)$$

where $\mu = \frac{m_s^*}{m_f^*}$ and m_s^* (m_f^*) is the effective mass in the semiconductor (ferromagnet). Here, we have made use of the fact that α_R (and therefore k_R) is zero in the ferromagnetic contacts so that a term containing $k_R(-\epsilon)$ does not appear in Eq.(23). This last equation ensures continuity of the current density at the ferromagnetic contact/semiconductor interface [17].

1.3 The interface conductance

At $T = 0$ K, the conductance of the interface is calculated using the Landauer formula, i.e., the sum over the majority and minority spin subbands of e^2/h times the transmission coefficient across the interface for each subband. For each subband, the transmission coefficient is the ratio of the current density in the semiconducting channel divided by the current density of the incident beam in the ferromagnetic contact.

The transmitted current density in the semiconductor channel is found by plugging Eq.(19) into the current density expression

$$J_x = \frac{\hbar}{2m^*i} \left(\Psi^\dagger \frac{d\Psi}{dx} - \frac{d\Psi^\dagger}{dx} \Psi \right) + \frac{\alpha_R}{\hbar} (\Psi^\dagger \sigma_z \Psi) \quad (24)$$

For electron with incident energy within the energy range $[E_2, E_3]$ where one of the mode is evanescent in the channel, this leads to

$$\begin{aligned} J_x &= \frac{\hbar}{m^*} \left[|T_1|^2 (k_{x,1} + k_R(|C_1|^2 - |C'_1|^2)) + |T_2|^2 k_R(|C_2|^2 - |C'_2|^2) \right] \\ &+ \frac{2\hbar k_R}{m^*} \text{Re} [T_2 T_1^* (C_2 C_1^* - C'_2 C'_1^*)] \\ &+ \frac{\hbar}{m^*} \text{Re} [T_2 T_1^* (C_2 C_1^* + C'_2 C'_1^*) (i\kappa + k_{x,1})], \end{aligned} \quad (25)$$

where the \star stands for complex conjugate.

At $T = 0$ K, the conductance of the interface due to the majority spin band is then given by

$$G_\uparrow = \frac{e^2}{h} T_\uparrow = \frac{e^2}{h} (J_x / J_x^{inc}) \quad (26)$$

where $J_x^{inc} = \hbar k_x^u / m_o$. A similar calculation yields G_\downarrow . As a check of our numerical simulations, we also compute the total reflection coefficient for electrons incident in the majority spin band

$$R_\uparrow = |R_1|^2 + \frac{k_x^d}{k_x^u} |R_2|^2, \quad (27)$$

and electrons incident in the minority spin band

$$R_\downarrow = \frac{k_x^u}{k_x^d} |R_1|^2 + |R_2|^2, \quad (28)$$

and check numerically that $R_\uparrow + R_\downarrow + T_\uparrow + T_\downarrow = 1$.

The last term in Eq.(25) is proportional to the overlap factor $(C_2 C_1^\star + C'_2 C'_1^\star)$ between the two eigenspinors in the channel and is non-zero in the presence of an axial magnetic field which makes the two spinors (at a given energy) non-orthogonal. This is an important feature which leads to the presence of antiresonances in the transmission coefficient of electrons incident in the minority spin band, as discussed in the next section. Since the two spinors are non-orthogonal only if there is (i) an axial magnetic field, and (ii) a spin orbit interaction in the semiconductor, it is obvious these two conditions are necessary for the anti-resonances to occur. Accordingly, the effect reported in this paper, namely 100% spin injection efficiency caused by anti-resonances, requires a magnetic field and spin-orbit interaction.

2 Results and discussions

We consider a Fe/Sm quantum wire interface with the geometry shown in Fig. 1 and with the parameters listed in Table I. The electrostatic confinement along the z-direction is assumed to be parabolic with $\hbar\omega = 10$ meV.

For simplicity, we assume that the Rashba spin-orbit coupling constant α_R and the strength V_0 of the Schottky barrier height at the Fe/Sm quantum wire interface are independent of the gate potential. For an interface with the parameters listed in Table I, the critical magnetic field B_c below which the E- k_x relationship for the lowest

propagating mode in the semiconducting channel has a camelback shape is equal to 0.07 Tesla. Figure 3 is a plot of the magnetic field dependence of the threshold energies (E_1, E_2, E_3).

Figure 4 is a plot of the wavevectors in the two subbands corresponding to the Fermi energy as a function of the electron incident energy for an external magnetic field of 0.02 T (which is below) and 0.2 T (which is above) the critical value B_c (0.07 T). Figure 4(a) shows that the top subband becomes evanescent when the Fermi level in the contact falls within the energy range $[E_2, E_3]$. In this energy range, $k_{x,2}$ is purely imaginary and we have plotted in Fig.4 the quantity κ such that $k_{x,2} = i \kappa$. Note that κ is exactly zero at E_2 and E_3 as can easily be shown using the equations derived in Section 1.1. Furthermore, κ reaches a maximum in the energy range $[E_2, E_3]$ which can be shown to be located at an energy E^* given by

$$E^* = \frac{\hbar\omega}{2} + \Delta E_c - \frac{\beta^2}{4\delta_R}. \quad (29)$$

When $B > B_c$ as in Fig.4(b), $k_{x,2}$ is purely imaginary in the energy range $[E_1, E_3]$ and we also plot the value of κ such that $k_{x,2} = i \kappa$ in that interval.

Figures 5 and 6 show plots of the conductance (in units of e^2/h) variation with ΔE_c for the case where the longitudinal magnetic field is equal to 0.02 T ($< B_c$) and 0.2 T ($> B_c$), respectively. Figure 5 shows an abrupt drop in the conductance from a finite value down to zero as the Fermi level in the contact is brought below the threshold energy E_1 shown in Fig.2(a). As discussed in Section 1, the sudden drop is related to the fact that, right at the threshold energy, the wavevector of the two free propagating modes in the semiconductor channel are equal and non-zero. On the other hand, the conductance goes down *smoothly* to zero when $B > B_c$ (Fig. 6) since the wavevector of the only propagating mode vanishes when E_F crosses the threshold energy E_1 in Fig. 2(b).

Figures 5 and 6 show that the conductance of the interface depends strongly on the strength of the Schottky barrier height V_0 , with larger values leading to a

smaller conductance. When the magnetic field is above B_c as in Fig.6, there is a kink in the conductance appearing at the energy where the upper subband becomes evanescent (Zeeman energy E_3 in Fig.2(b)). When $B < B_c$, the upper subband is only evanescent when the Fermi energy is within the energy range $[E_2, E_3]$ (See Fig.4(a)). The conductance reaches a minimum at the edges of this energy range and shows another kink within the interval at the energy E^* given by Eq.(29). Also shown in Figures 5 and 6 is G_{tot} versus ΔE_c when there is no axial magnetic field in the channel (for the case $V_0 = 0$ eV Å). In this case, G_{tot} is a smooth function of ΔE_c and goes down to zero smoothly at threshold. This feature is found to be independent of the Schottky barrier strength at the interface. In the absence of an externally applied magnetic field, the presence of kinks in the interface conductance at low temperature highlights the non-trivial effect that a stray magnetic field in the channel has.

The kink in Fig.5 and the local minima in G_{tot} in Fig. 6 are due to antiresonances in the transmission coefficient of the minority spin band when the Fermi level in the ferromagnetic contact is lined up with the Zeeman energy levels in the semiconductor channel, as illustrated in Figures 7 and 8, for $B < B_c$ and $B > B_c$, respectively. At zero temperature, these antiresonances lead to a *perfect* ($\eta = 100\%$) spin injection efficiency, as illustrated in Figs. 10 and 11 for the case of $B < B_c$ and $B > B_c$, respectively. One important feature is that this perfect spin injection efficiency is *independent* of the value of the Schottky barrier height. This means that no Schottky barrier or tunnel barrier is necessary to implement the 100% spin injection efficiency. Perfect spin filtering (or 100% spin injection efficiency, i.e. $\eta = 1$) occurs when the Fermi level E_F in the ferromagnetic contact coincides with E_2 or E_3 levels in the channel when $B < B_c$ and when E_F coincides with E_3 when $B > B_c$.

2.1 Importance of the magnetic field

For both $B < B_c$ and $B > B_c$, $[C_2(k_{x,2}), C'_2(k_{x,2})]^T$ (where T stands for transpose) reduces to $\frac{1}{\sqrt{2}}[1, -1]$ when the Fermi level in the contact coincides with E_2 or E_3 . On the other hand, $[C_1(k_{x,1}), C'_1(k_{x,1})]^T$ is not equal to $\frac{1}{\sqrt{2}}[1, 1]$ at either E_2 or E_3 , when $B < B_c$, but it is equal to $\frac{1}{\sqrt{2}}[1, 1]$ at E_2 when $B > B_c$.

When $B < B_c$, the overlap factor in Eq.(24) is non-zero when $E_F = E_2$ or E_3 . In this case, it can be shown that both T_1 and T_2 in Eq.(25) are non-zero at these incident energies for electrons incident in both majority and minority spin bands. Furthermore, in the case of minority spin band, the contribution from the overlap term in Eq.(25) exactly cancels the other contributions leading to zero transmitted current in the channel [21].

When $B > B_c$, $T_1 = T_2 = 0$ for both minority and majority spin bands incident from the contact when $E_F = E_2$. In that case the 4x4 system of equations reduces to two 2x2 systems of equations with no mixing between the two subbands in the channel.

The maximum spin injection efficiency is much less than 100% and virtually independent of ΔE_c when the axial magnetic is assumed to be *zero*, as illustrated by the dashed line in Figures 9 and 10. In that case, the spin subbands are orthogonal in the channel and there is no antiresonance in the transmission coefficient of the minority spins. Thus, the axial magnetic field is critical to ensure perfect spin filtering and 100 % spin injection efficiency!

2.2 Role of tunnel barrier

Another important feature in Figures 10 and 11 is that over a given range of ΔE_c , (or, equivalently, over a range of injection energies), the spin injection efficiency is larger if the Schottky barrier height at the interface is larger. This means that although no barrier is required for perfect spin filtering at $T = 0$ K, a barrier is beneficial at T

$> 0\text{K}$ when thermal smearing causes a spread in the injection energy. The presence of a taller barrier leads to improved spin filtering over a *range of energies*. This is consistent with the result of ref. [9]. The difference with ref. [9] is that we consider *ballistic* transport whereas ref. [9] considered *diffusive* transport. Thus, we have extended the basic finding of ref. [9] to the regime of ballistic transport.

2.3 Transconductance

Since the quantum wire will be typically formed using a split-gate, a more negative voltage on the gate will lead to an increase of ΔE_c . Fig.5 shows that, at very low temperature when $B < B_c$, there are regimes of operation where the transconductance, dG_{tot}/dV_G , can be either positive or negative. In contrast, it is always positive when $B > B_c$, as shown in Fig. 6. Since the regime of negative transconductance occurs over a very narrow range of ΔE_c , they can only be observed at very low temperature. This is illustrated in Fig.9(a) where G_{tot} is plotted versus ΔE_c as a function of temperature when $B < B_c$. Figure 9(b) also shows that the kink in G_{tot} , appearing when $B > B_c$, is rapidly smoothed out as the temperature increases. Even though not shown here, the curves for G_{tot} in Figures 9(a) and 9(b) at non-zero temperature were found to smoothly reach zero at larger values of ΔE_c .

2.4 Temperature dependence of the spin injection efficiency

The spin injection efficiency decreases rapidly as the temperature increases, especially when the axial magnetic field is below the critical magnetic field value B_c . For devices with GaAs, InAs, or InSb semiconducting channels operating with a value of the Rashba spin-orbit coupling constant α_R equal to 10^{-11} eV cm, B_c is equal to 6.89, 0.07, and 0.012 Tesla, respectively. Figures 12 and 13 show that the maximum spin injection efficiency rapidly degrades as the temperature rises. The degradation is faster when the axial magnetic field is below the critical value B_c . For instance, at $T = 0.1$ K, the spin injection efficiency is still around 82 % when $B > B_c$ whereas it is

down to 12 % when $B < B_c$.

This can be understood as follows. In the Landauer-Büttiker formalism, the linear response conductance is given by Eq.(1) and is a convolution over energy of the transmission coefficient and the bell shape function (sech^2) centered just a few $k_B T$ around the Fermi level. As illustrated in Figures 9(a) and 9(b), the transmission coefficient of the minority spin band in the energy range $[E_1, E_F + 2k_B T]$ is smaller when $B > B_c$ compared to the case when $B < B_c$. Therefore, the contribution to the conductance due to minority spins will be less when $B > B_c$. This leads to a less rapid decrease of the spin injection efficiency with temperature when $B > B_c$.

An estimate of the temperature T^* at which the spin injection efficiency will decrease substantially can be obtained from the equation,

$$4k_B T^* = |g^*| \mu_B B, \quad (30)$$

which equates the approximate width of the bell shaped function (sech^2) in Eq.(1) to the splitting between the two Zeeman energy states in the channel. Table II lists T^* for different semiconductor materials and two different values of the axial magnetic field. This table indicates that a larger spin injection efficiency should be sustainable at higher temperature in devices based on InSb channels. Table II also indicates that a rapid decrease of the spin injection efficiency is expected at a temperature of 0.05 K and 0.5 K when $B < B_c$ and $B > B_c$, respectively, in agreement with the plots shown in Figures 12 and 13.

2.5 Structure for maintaining a large spin injection efficiency at elevated temperatures

It is obvious that the degradation of the spin injection efficiency at elevated temperatures is caused by the thermal smearing of the injection energy around the critical value. The remedy to this problem is to interpose a double barrier resonant tunneling diode between the ferromagnet and the semiconductor quantum wire as shown

in Fig.14. The barrier heights and widths are chosen to be sufficiently large so that there is a narrow transmission peak at the resonant energy. All we have to do is design the double barrier structure such that the resonance energy is matched to the critical injection energy needed to achieve a 100% spin injection efficiency. In that case, a nearly monochromatic beam of electrons is incident on the semiconductor structure at the critical energy and this will lead to a high spin injection energy, even at relatively elevated temperatures.

3 Conclusions

We have shown that at $T = 0$ K, 100% spin injection efficiency is possible across the interface of a non-ideal metallic ferromagnet and a semiconductor quantum wire, without a tunnel barrier, provided we inject carriers with certain energies. Additional requirements are that there must be an axial magnetic field and a spin orbit interaction in the quantum wire. We have also described some approaches to retaining a high spin injection efficiency at elevated temperatures by designing appropriate structures and choosing appropriate semiconductor materials.

The work at Virginia was supported by the Air Force Office of Scientific Research under grant FA9550-04-1-0261.

Table I: Parameters of Fe/InAs interface

Fermi Energy E_F (eV)	4.2
Exchange splitting energy Δ (eV)	3.46
Rashba spin-orbit coupling constant α_R (10^{-11} eVcm)	1.
Lande Factor g^* [22]	-14.9
Effective mass m_f^* in Fe contact (m_0)	1.
Effective mass m_s^* in InAs channel (m_0) [22]	0.023

Table II: Critical temperature T^* (Kelvin)
for different semiconductor channels

Axial magnetic field (Tesla)	GaAs	InAs	InSb
0.02	0.0015	0.05	0.17
0.2	0.015	0.5	1.73

References

- [1] H.J. Zhu, M. Ramsteiner, H. Kostial, M. Wassermeier, H.-P. Schönherr, and K.H. Ploog, Phys. Rev. Lett. 87, 016601 (2001).
- [2] A.T. Hanbicki, B.T. Jonker, G. Itskos, G. Kioseoglou, and A. Petrou, Appl. Phys. Lett. 80, 1240 (2002).
- [3] A.T. Hanbicki, O.M.J. van't Erve, R. Magno, G. Kioseoglou, C.H. Li, B.T. Jonker, G. Itskos, R. Mallory, M. Yasar and A. Petrou, Appl. Phys. Lett. 82, 4092 (2003).
- [4] V.F. Motsnyi, J. De Boeck, J. Das, W. Van Roy, G. Borghs, E. Goovaerts, and V.I. Safarov, Appl. Phys. Lett. 81, 265 (2002).
- [5] T. Manago and H. Akinaga, Appl. Phys. Lett. 81, 265 (2002).
- [6] G. Salis, R. Wang, X. Jiang, R. M. Shelby, S. S. P. Parkin, S. R. Bank and J. S. Harris, Appl. Phys. Lett. 87, 262503 (2005).
- [7] S.H. Chun, S.J. Potashnik, K.C. Ku, P. Schiffer, and N. Samarth, Phys. Rev. B 66, R100408 (2002).
- [8] C.-M. Hu and T. Matsuyama, Phys. Rev. Lett 8, 066803-1 (2001).
- [9] E.I. Rashba, Phys. Rev. B 62, R16267 (2000).
- [10] L.W. Molenkamp, G. Schmidt, and G.E.W. Bauer, Phys. Rev. B 64, 121202 (2001).
- [11] M. Zwierzycki, K. Xia, P.J. Kelly, G.E.W. Bauer, and I. Turek, arXiv:cond-mat/0204422 (2002).
- [12] O. Wunnicke, Ph. Mavropoulos, R. Zeller, and P.H. Dederichs, and D. Grundler, Phys. Rev. B 65, 241306(R) (2002).

- [13] G. Schmidt, D. Ferrand, L. W. Molenkamp, A. T. Filip and B. J. van Wees, Phys. Rev. B 62, R4790 (2000).
- [14] E. I. Rashba, Sov. Phys. Semicond., Vol. 2, 1109 (1960); Y. A. Bychkov and E. I. Rashba, J. Phys. C 17, 6039 (1984).
- [15] S. Datta and B. Das, Appl. Phys. Lett. 56, 665 (1990).
- [16] M. Cahay and S. Bandyopadhyay, Phys. Rev. B 68, 115316 (2003); S. Bandyopadhyay, S. Pramanik and M. Cahay, Superlat. Microstruct. 35, 67 (2004).
- [17] M. Cahay and S. Bandyopadhyay, Phys. Rev. B 69, 045303 (2004).
- [18] For the most commonly studied III-V semiconductor materials for spintronics applications (GaAs, InAs, and InSb), the g^* values for bulk samples are negative and equal to -0.44, -14.9, and -51.0, respectively.
- [19] J. Nitta, T. Akazaki, H. Takayanagi, and T. Enoki, Phys. Rev. Lett. 78, 1335 (1997); G. Engels, J. Lange, Th. Schäpers, and H. Lüth, Phys. Rev. B 55, 1958 (1997); Th. Schäpers, G. Engels, J. Lange, Th. Klocke, M. Hollfelder, and H. Lüth, J. Appl. Phys. 83, 4324 (1998); C.-M. Hu, J. Nitta, T. Akazaki, H. Takayanagi, J. Osaka, P. Pfeffer, and W. Zawadzki, Phys. Rev. B 60, 7736 (1999); J.P. Heida, B.J. van Wees, J.J. Kuipers, T.M. Kalpwaik, and G. Borghs, Phys. Rev. B 57, 11911 (1998); S. Brosig, K. Ensslin, R.J. Warburton, C. Nguyen, B. Brar, M. Thomas, and H. Kroemer, Phys. Rev. B 60, 13989 (1999); H.B. Heersche, Th. Schäpers, J. Nitta, and H. Takayanagi, Phys. Rev. B 64, 161307 (2001). Y. Sato, T. Kita, S. Gozu and S. Yamada, J. Appl. Phys. 89, 8017 (2001); Y. Sato, S. Gozu, T. Kita and S. Yamada, Physica E 12, 399 (2002).
- [20] Th. Schäpers, J. Nitta, H.B. Heersche, and H. Takayanagi, Phys. Rev. B 64, 125314 (2001).

- [21] J. Wan, M. Cahay and S. Bandyopadhyay (unpublished notes).
- [22] G. Papp and F.M. Peeters, *Appl. Phys. Letters* 78, 2184 (2001).
- [23] F.G. Pikus and G.E. Pikus, *Phys. Rev. B* 51, 16928 (1995).
- [24] P. Pfeffer and W. Zawadzki, *Phys. Rev. B* 68, 035315 (2003).
- [25] W. Zawadzki and P. Pfeffer, *Semicond. Sci. Technol.* 19, R1-R17 (2004).

Figure Captions

Figure 1: Ferromagnetic/semiconducting quantum wire contact. (a) Top view of the structure showing the ferromagnetic contact with its magnetization in the direction of current flow in the quantum wire. An external magnetic field is applied along the direction of the wire. The conductance of the wire is measured between the ferromagnetic source and a (non-magnetic) drain contact located in the two-dimensional electron gas on the right. (b) Cross-sectional view of the structure showing as a thick dashed line the quasi one-dimensional electron gas in the wire.

Figure 2: Energy band diagram across the ferromagnetic contact/semiconductor quantum wire interface. We use a Stoner-Wohlfarth model for the ferromagnetic contact. Δ is the exchange splitting energy in the contacts. ΔE_c is the height of the potential barrier between the energy band bottoms of the semiconductor and the ferromagnetic contacts. Also shown are the energy dispersion relationships on both sides of the interface for the case of an axial magnetic field (along the x-direction of current flow shown in Fig.1) below (top figure) or above (bottom figure) the critical magnetic field value discussed in the text.

Figure 3: Magnetic field dependence of the energies E_1 , E_2 , and E_3 (from bottom to top) versus magnetic field for a quantum wire with the parameters listed in Table I. For $B > B_c$ (0.07 T in our simulations), $E_1 = E_2$.

Figure 4: Energy dependence of the wavevectors in the two lower subbands for a magnetic field of $B = 0.02$ T which is below the critical value $B_c = 0.07$ T (top figure) and for $B = 0.2$ T which is above B_c (bottom figure). The interface parameters are listed in Table I. The threshold energies E_1 , E_2 , and E_3 discussed in section II are indicated. In the energy range where the upper subband becomes evanescent, we have plotted κ , where $k_{x,2} = i \kappa$ with $k_{x,2}$ given by Eq.(14). The wavevectors are plotted

in units of the Rashba wavevector k_R .

Figure 5: Zero temperature variation of the conductance (in units of e^2/h) of a ferromagnetic contact/semiconducting nanowire as a function of ΔE_c for a magnetic field $B = 0.02$ T which is below the critical value B_c given by Eq.(10). The different full lines correspond to different values of V_0 characterizing the strength of the Schottky barrier height at the ferromagnet/semiconductor interface. From top to bottom, $V_0 = 0, 1$, and 2 eV \AA , respectively. Also shown as a dashed line is G_{tot} versus ΔE_c neglecting the axial magnetic field in the channel for $V_0 = 0$ eV \AA .

Figure 6: Same as Fig.5 for an axial magnetic field of 0.2 Tesla.

Figure 7: Energy dependence of the total transmission coefficient of minority (T_\downarrow , full lines) and majority (T_\uparrow , dashed lines) spin bands across the ferromagnetic contact/semiconductor quantum wire interface over the energy range [$E_1, E_F + 2k_B T$] for $T = 2$ K. The axial magnetic field is equal to 0.02 T. For each set of curves, the strength of the Schottky barrier height V_0 from top to bottom is equal to 0, 1, and 2 eV \AA , respectively.

Figure 8: Same as Fig.7 for an axial magnetic field of 0.2 T.

Figure 9: Conductance (in units of e^2/h) of a ferromagnetic contact/semiconducting quantum wire as a function of ΔE_c and temperature. The strength V_0 of the Schottky barrier height at the ferromagnet/semiconductor interface is set equal to 1 eV \AA . The top and bottom figures are for an axial magnetic field in the quantum wire equal to 0.02 and 0.2 Tesla, respectively.

Figure 10: Zero temperature variation of the spin injection efficiency of a ferromagnetic contact/semiconducting quantum wire interface as a function of ΔE_c for a magnetic field $B = 0.02$ T. The different full lines correspond to different values of V_0 characterizing the strength of the Schottky barrier height at the ferromagnet/semiconductor interface. The dashed lines are the spin injection efficiency calcu-

lated with no axial magnetic field in the channel. For both sets of curves, $V_0 = 0, 1$, and $2 \text{ eV}\text{\AA}$, from bottom to top.

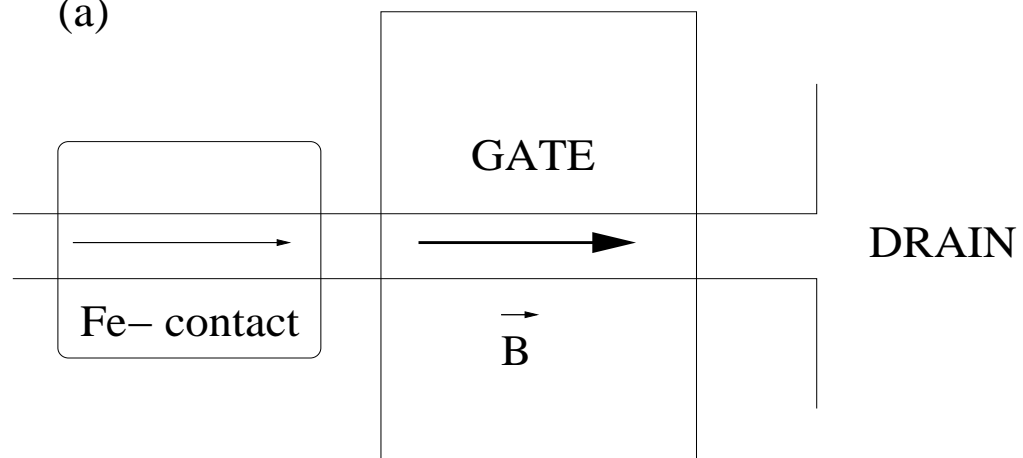
Figure 11: Same as Fig.10 for an axial magnetic field $B = 0.2 \text{ T}$.

Figure 12: Temperature variation of the spin injection efficiency of a ferromagnetic contact/semiconducting quantum wire interface as a function of ΔE_c for a magnetic field $B = 0.2 \text{ T}$. From top to bottom, the different curves correspond to a temperature of 0, 0.1, 0.5, 1, and 2 K, respectively. The strength of the Schottky barrier height V_0 at the ferromagnet/semiconductor interface is set equal to $1 \text{ eV}\text{\AA}$.

Figure 13: Same as Fig.12 for an axial magnetic field of 0.2 T .

Figure 14: Proposed double barrier resonant tunneling heterostructure to maintain efficient spin injection at elevated temperatures.

(a)



(b)

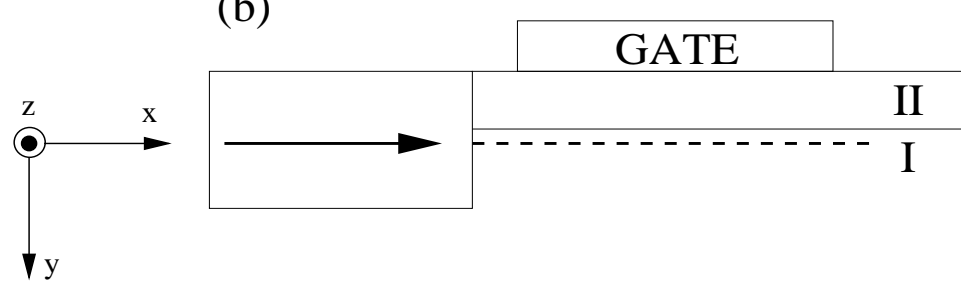


Figure 1

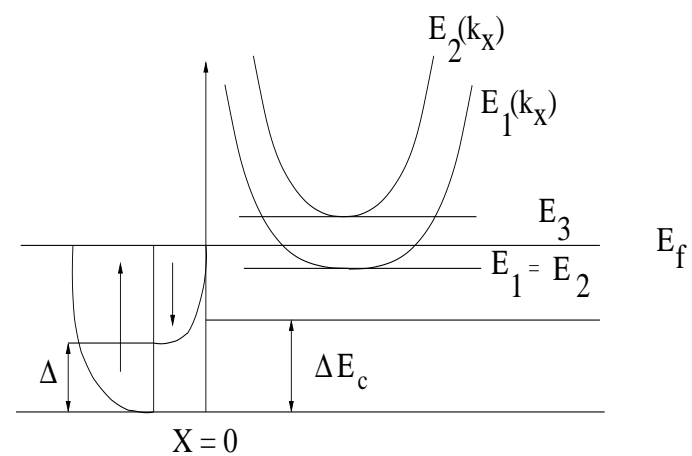
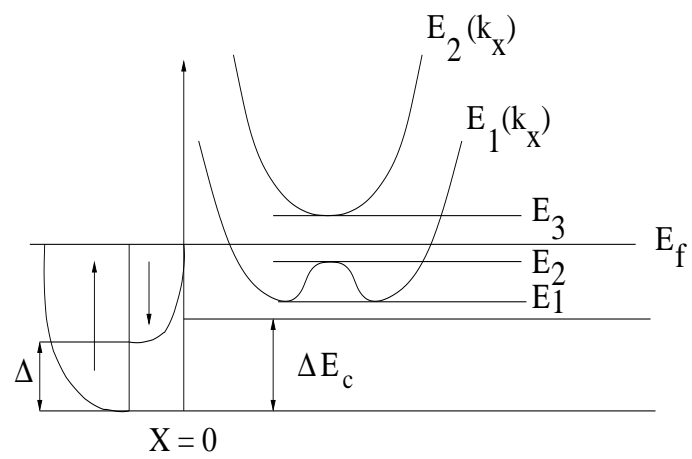


Figure 2

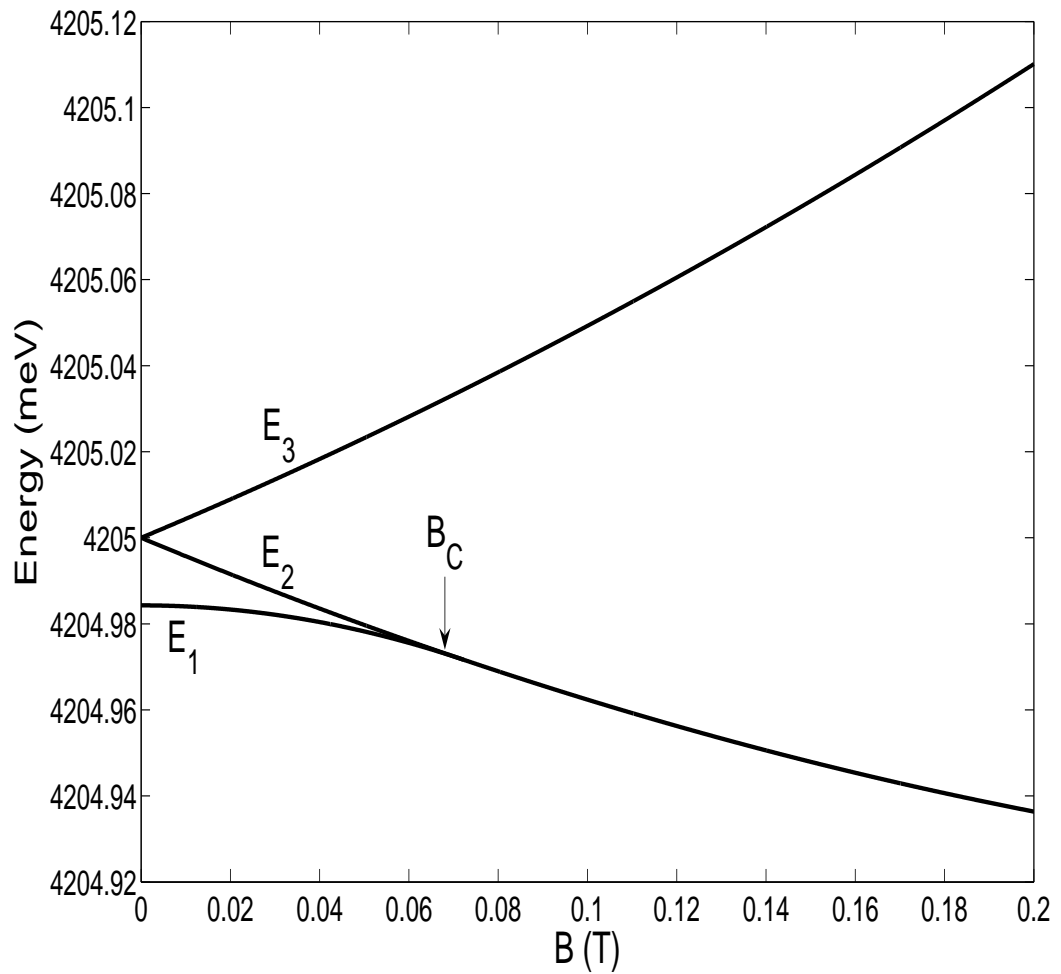


Figure 3

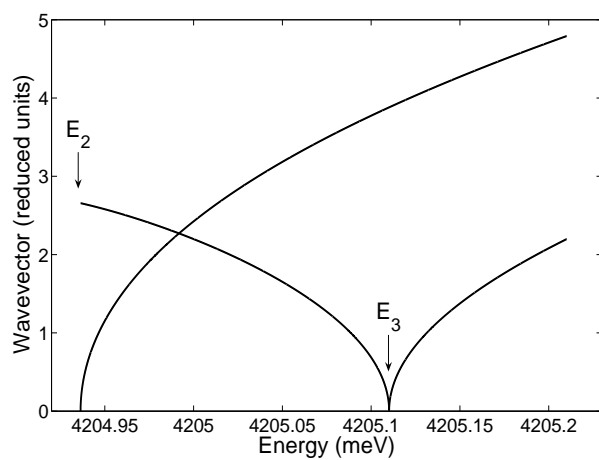
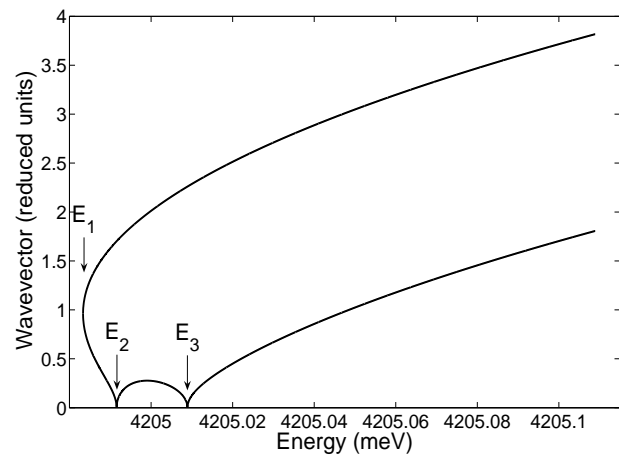


Figure 4

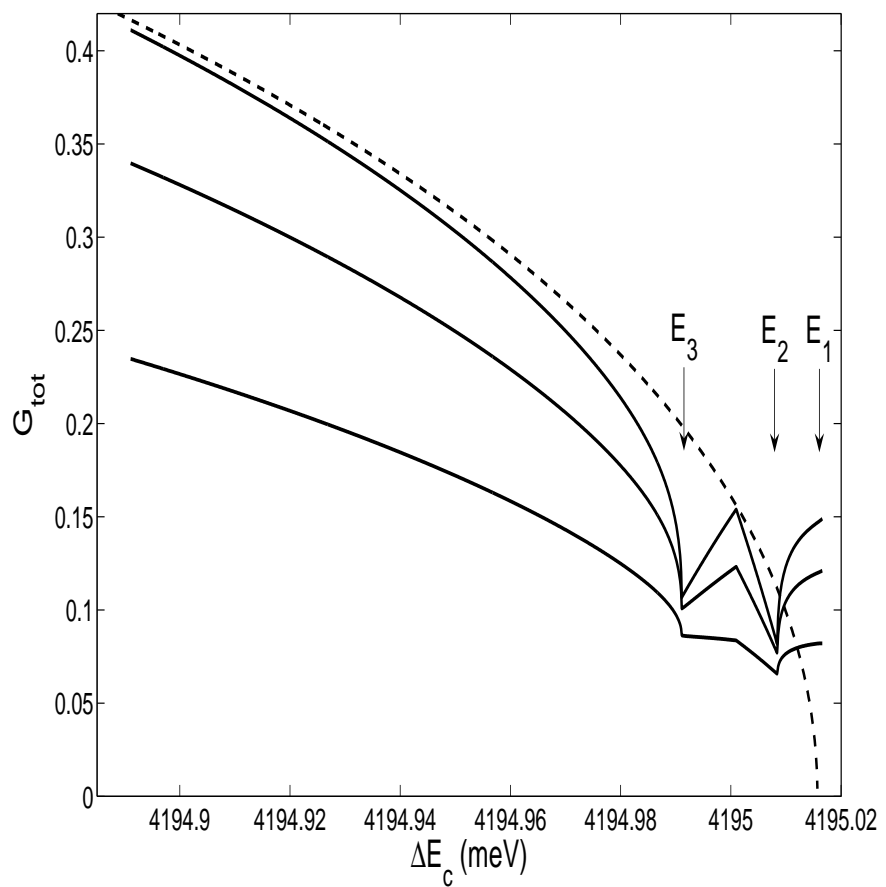


Figure 5

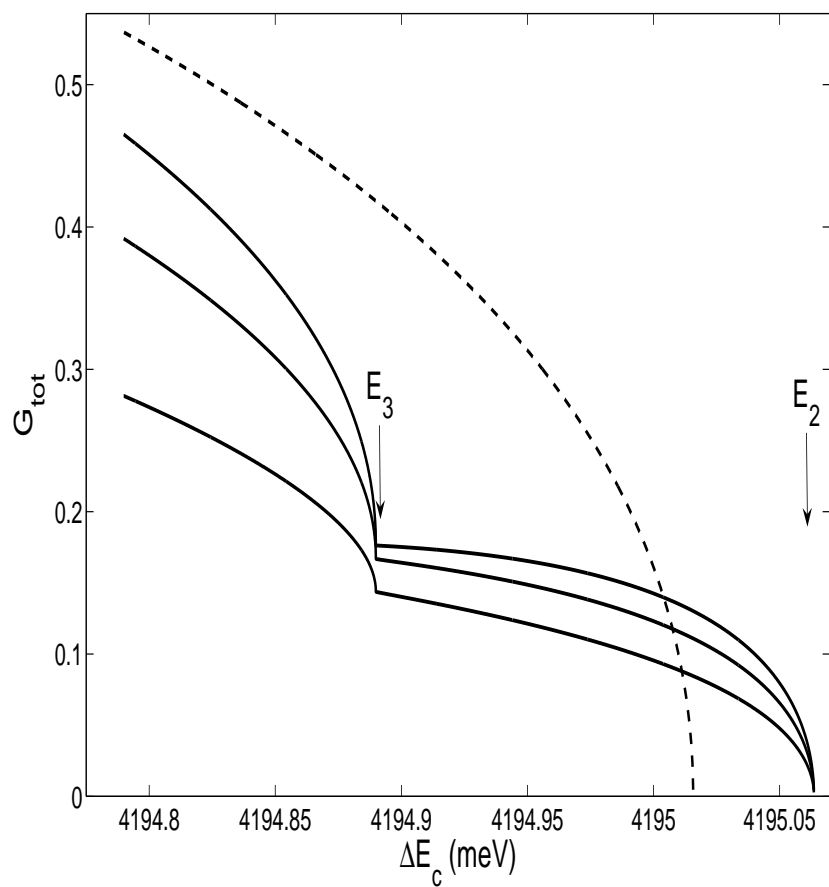


Figure 6

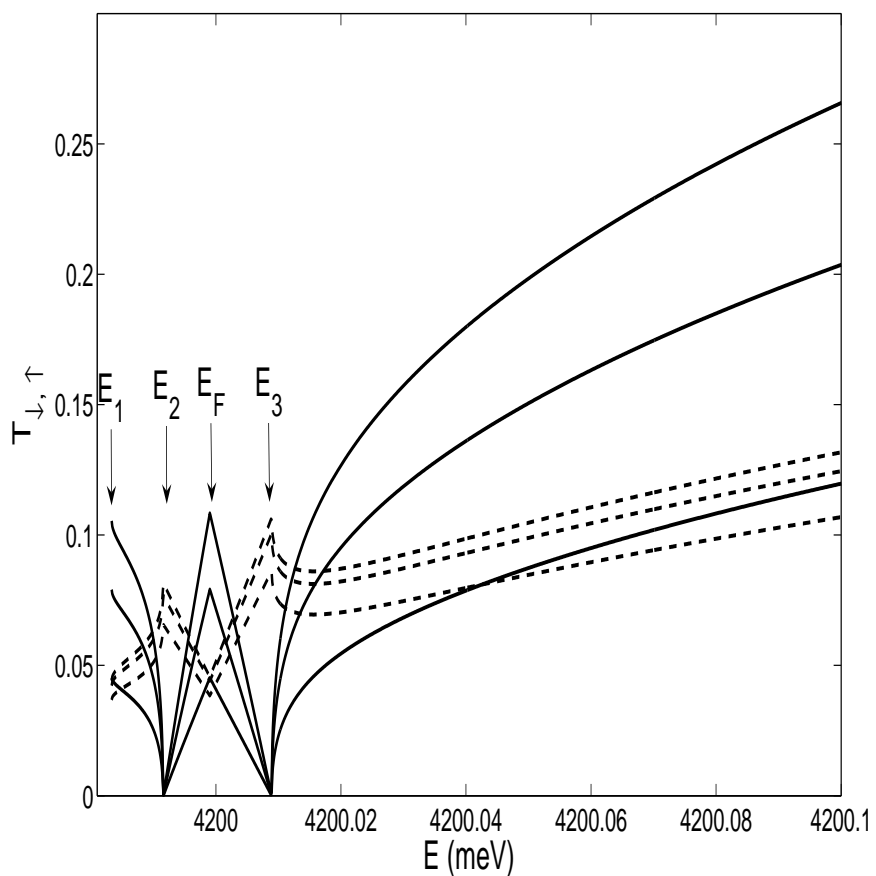


Figure 7

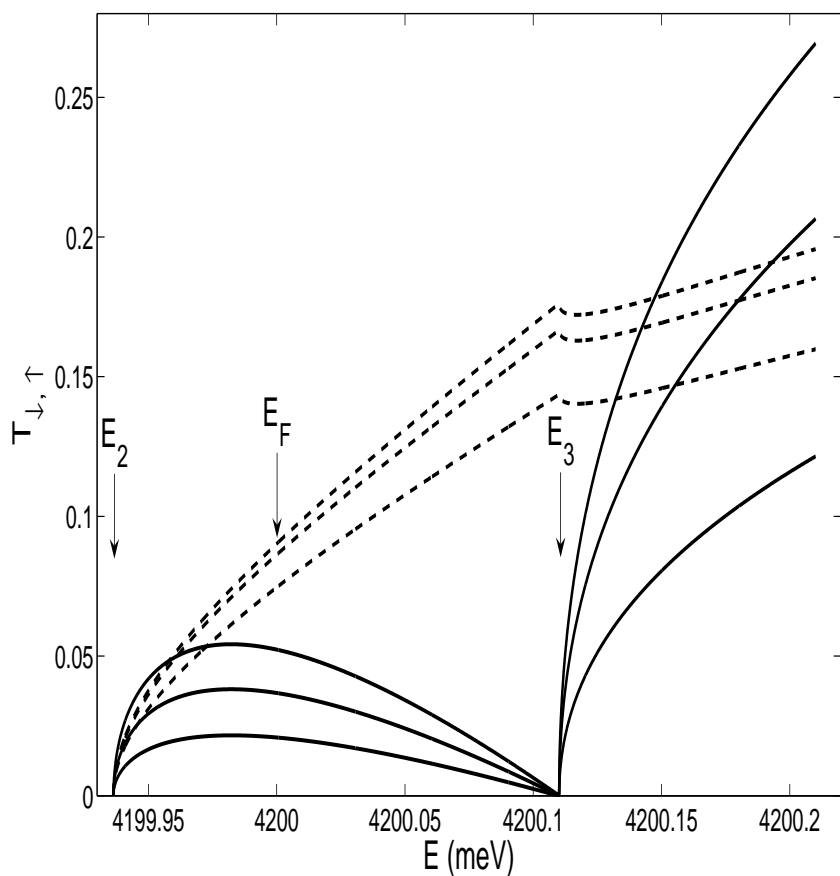


Figure 8

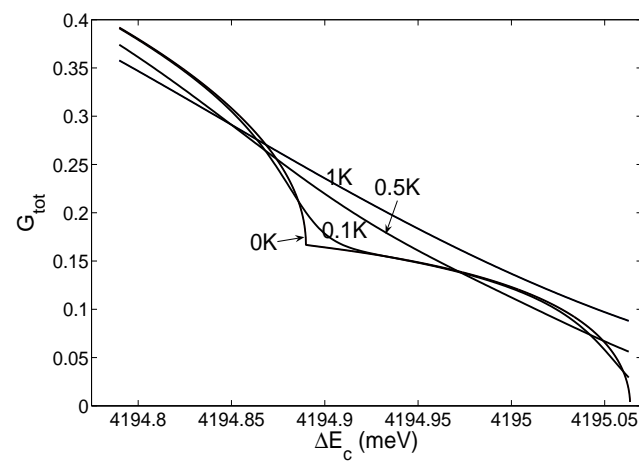
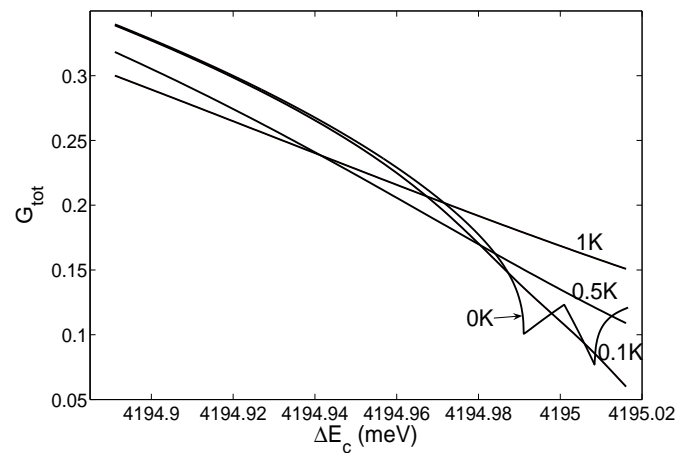


Figure 9

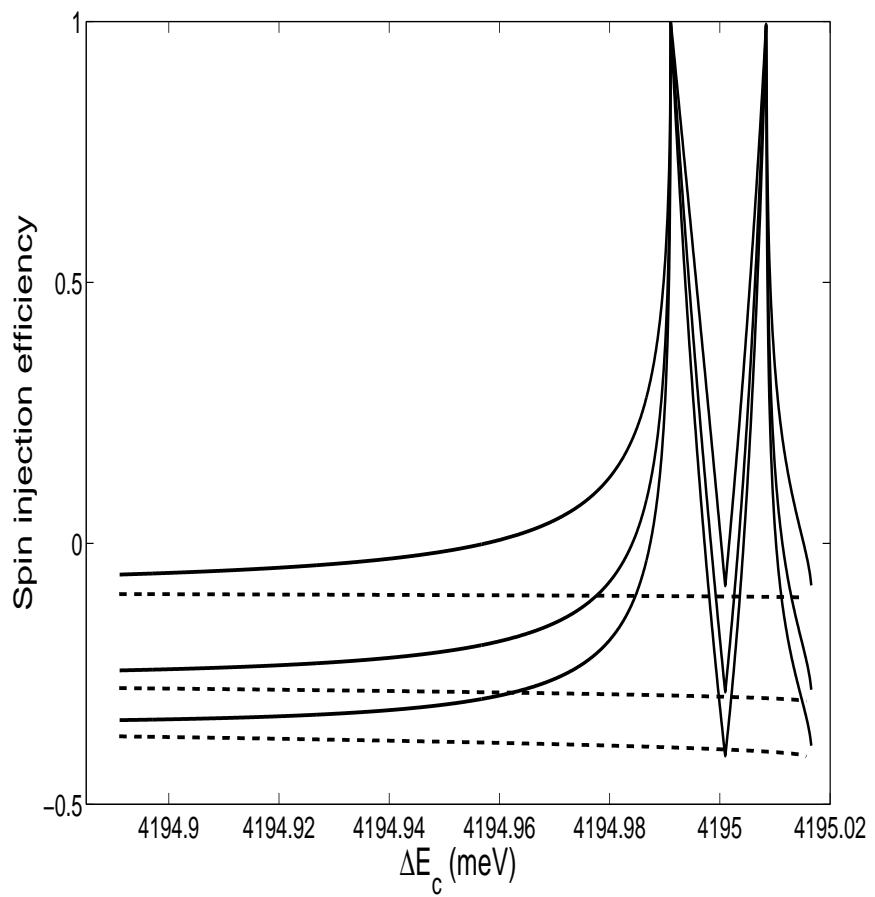


Figure 10

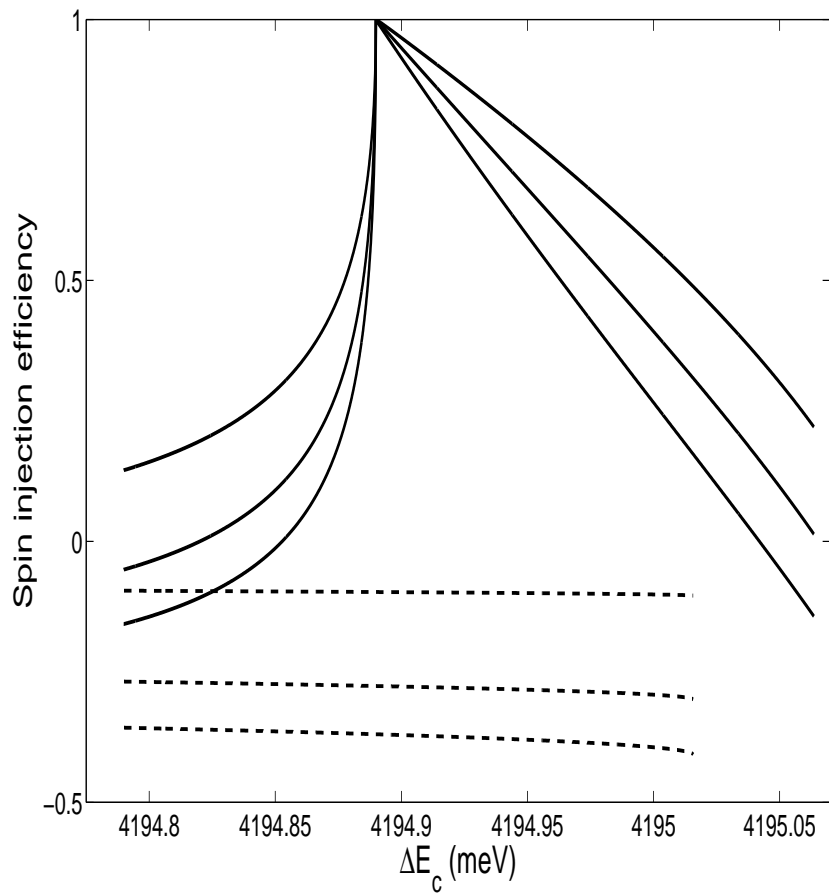


Figure 11

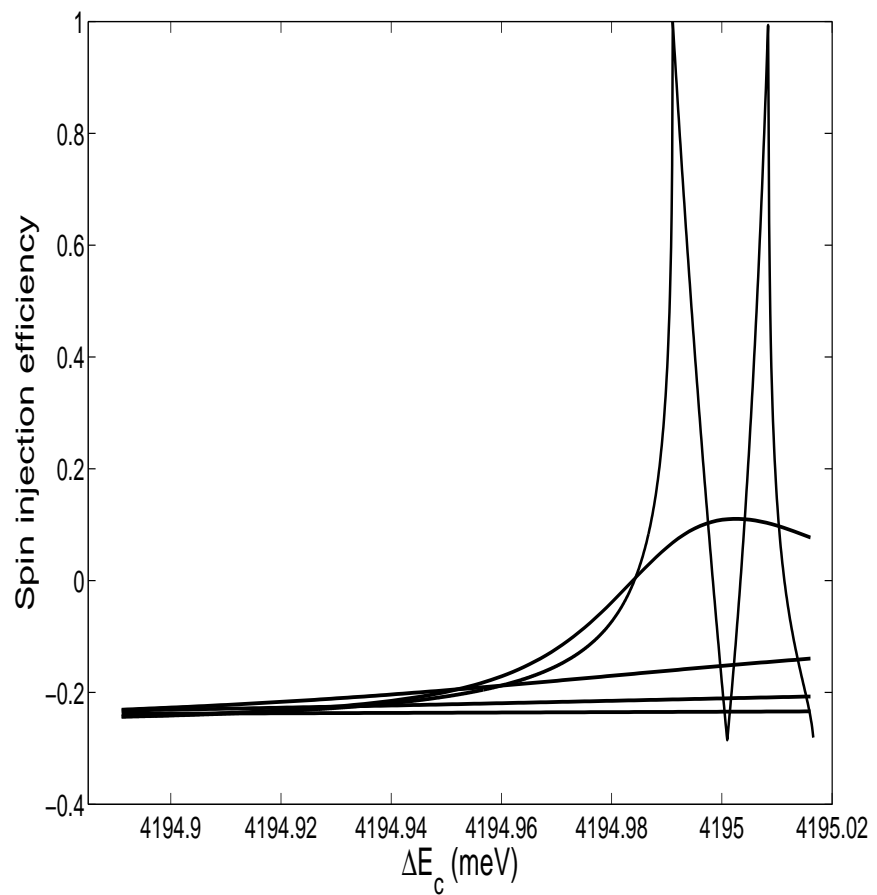


Figure 12

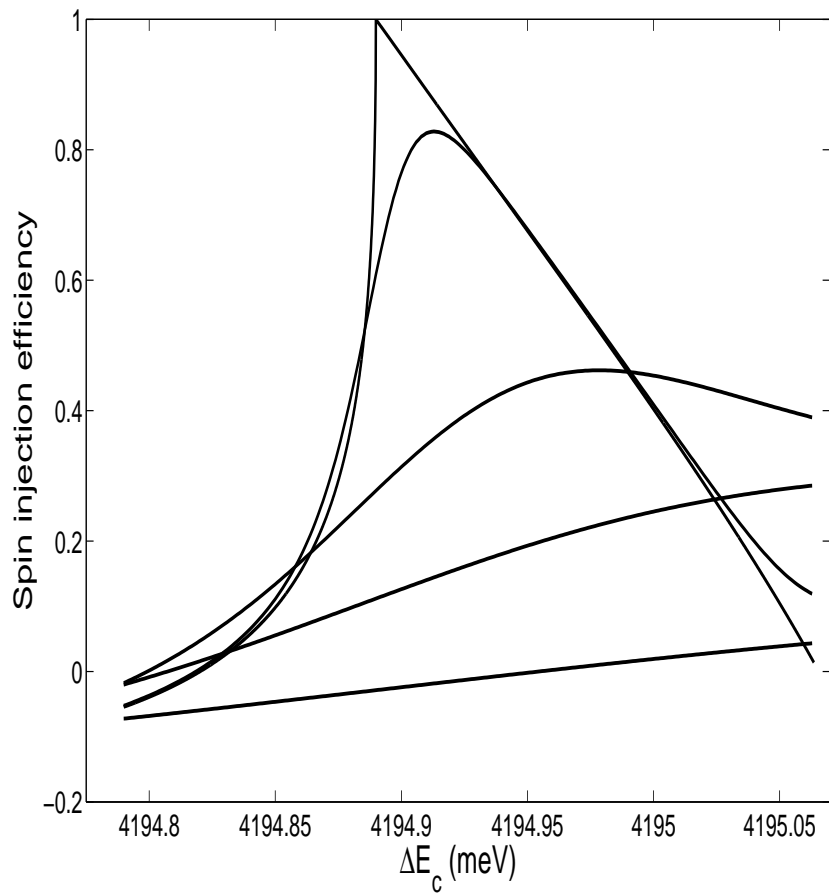
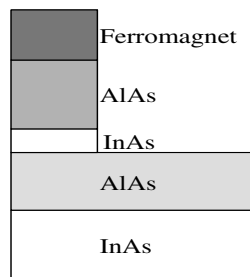
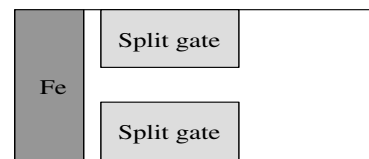


Figure 13



Side View



Top View

Figure 14